

High-Resolution fMRI Using Multislice Partial k -Space GR-EPI With Cubic Voxels

James S. Hyde,* Bharat B. Biswal, and Andrzej Jesmanowicz

The premises of this work are: 1) the limit of spatial resolution in fMRI is determined by anatomy of the microcirculation; 2) because of cortical gray matter tortuosity, fMRI experiments should (in principle) be carried out using cubic voxels; and 3) the noise in fMRI experiments is dominated by low-frequency BOLD fluctuations that are a consequence of spontaneous neuronal events and are pixel-wise dependent. A new model is proposed for fMRI contrast which predicts that the contrast-to-noise ratio (CNR) tends to be independent of voxel dimensions (in the absence of partial voluming of activated tissue), TE, and scanner bandwidth. These predictions have been tested at 3 T, and results support the model. Scatter plots of fMRI signal intensities and low-frequency fluctuations for activated pixels in a finger-tapping paradigm demonstrated a linear relationship between signal and noise that was independent of TE. The R^2 value was about 0.9 across eight subjects studied. The CNR tended to be constant across pixels within a subject but varied across subjects: $CNR = 3.2 \pm 1.0$. fMRI statistics at 20- and 40-ms TE values were indistinguishable, and TE values as short as 10 ms were used successfully. Robust fMRI data were obtained across all subjects using $1 \times 1 \times 1 \text{ mm}^3$ cubic voxels with 10 contiguous slices, although $1.5 \times 1.5 \times 1.5 \text{ mm}^3$ was found to be optimum. *Magn Reson Med* 46:114–125, 2001. © 2001 Wiley-Liss, Inc.

Key words: fMRI; neuroimaging; brain; physiological noise; BOLD contrast

PARTIAL VOLUME EFFECTS IN FMRI

This work is concerned with partial volume effects in human functional magnetic resonance imaging (fMRI), which is based on blood oxygenation level-dependent (BOLD) contrast. In functional imaging, the usual partial volume concept (i.e., smearing of anatomic features due to voxels that are too large) needs to be expanded. Within activated tissue, *functional* variation across space, including variation of percent enhancement and of the hemodynamic response waveform, can also occur. Spatial variation of functional parameters is partial volumed if the voxel size is too great.

Cortical gray matter exhibits considerable tortuosity, and it seems axiomatic that partial volume effects in fMRI can only be minimized by the use of cubic voxels. The issues then become, what is the optimum voxel size based on anatomy of the microcirculation, and can useful fMRI information be obtained using anatomically appropriate

voxels? In this work we first demonstrate fMRI acquisition over 10 contiguous 1-mm-thick slices with in-plane resolution of 1 mm^2 using single-shot partial k -space gradient-recalled echo-planar imaging (GR-EPI) (1) at 3T with a TR value typically of 2 s. A working hypothesis is developed that 1 mm^3 is both a practical volume and an anatomically rational volume for studies that are directed towards understanding fundamental aspects of fMRI contrast with minimal partial volume effects. This hypothesis is tested by systematic variation of the cubic voxel volume in a motor task. Results of these experiments lead to the conclusion that a somewhat larger voxel, $1.5 \times 1.5 \times 1.5 \text{ mm}^3$, is preferable from the perspective of optimum contrast-to-noise ratio (CNR).

CORTICAL CAPILLARY ANATOMY

Figure 52 in Duvernoy et al. (2) shows a cortical cross-section from the medial frontal gyrus with side-by-side labels for gray matter layers: 1) neuronal and 2) vascular. The highest capillary density occurs in vascular layer 3, which is 0.8 mm thick in this section. This layer corresponds to neuronal layers IIIc, IV, and V. It is generally supposed that the highest capillary density corresponds to the region of greatest metabolic demand. Presumably, the BOLD signal has its origin in vascular layer 3—possibly extending, as indicated in the figure, into adjacent layers. It is concluded that in the dimension that is perpendicular to the gray-matter surface, 1 mm is a desirable experimental level of resolution for investigation of BOLD contrast mechanisms.

Duvernoy et al. (2) classify intracortical penetrating veins into five groups. Group 3 penetrates to neuronal layer IV, group 4 to neuronal layer V, and group 5 (so-called principal veins) through to white matter. One may suppose that groups 3, 4, and 5 participate in BOLD contrast. These vessels are of progressively greater diameter, each fed by numerous branching capillaries in vascular layer 3. Duvernoy et al. (2) report diameters of 120–125 μ , 65 μ , and 45 μ for groups 5, 4, and 3, respectively. They describe rings of penetrating arteries surrounding the principal veins as well as veins in groups 3 and 4, and refer to these structures of arterial rings surrounding single veins as “venous units.” The number of penetrating arteries is much greater than the number of veins, and the larger the diameter of the veins the greater the number of penetrating arteries that surround it. The tangential area that is drained by veins in groups 3 and 4 ranges from 0.75 to 1 mm in diameter, while the area drained by principal veins ranges from 1 to 4 mm. It is concluded that $1 \times 1 \text{ mm}^2$ is a desirable experimental level of resolution in tangential cortical planes. Thus use of $1 \times 1 \times 1 \text{ mm}^3$ voxels simultaneously addresses the problems of gray-matter tortuosity

Biophysics Research Institute, Medical College of Wisconsin, Milwaukee, Wisconsin.

Grant sponsor: National Institutes of Health; Grant numbers: MH51358; CA41464; M01 RR00008-GCRC.

*Correspondence to: J.S. Hyde, Biophysics Research Institute, Medical College of Wisconsin, 8701 Watertown Plank Road, Milwaukee, WI 53226. E-mail: jshyde@mcw.edu

Received 1 February 2000; revised 4 January 2001; accepted 30 January 2001.

and of partial voluming of that portion of cortical tissue that can be expected to participate in BOLD contrast. The ultimate goal of our present line of research, of which this study is a first step, is to define those voxels that lie specifically in tissue from which the signal arises, and to define and suppress response from extracortical draining veins.

HIGH-RESOLUTION FMRI

High resolution can be achieved by the use of interleaved EPI (3–6) at the expense of temporal resolution. The partial k -space methods used here avoid this temporal compromise, permitting high-resolution spatial mapping of temporal characteristics. Hemodynamic delay and the hemodynamic response waveform are thought to arise from a cascade of the following steps: 1) release of one or more mediators in the central neuronal layers—for example, NO, K, and/or adenosine—during neuronal activity; 2) diffusion of mediators to smooth muscle cells on the arterial side; 3) vessel dilatation; and 4) blood transport to the observed voxel. Increased variability of temporal response can be expected as the spatial resolution increases, which we believe is important to study and which therefore provides a rationale for the emphasis on single-shot acquisition in this work.

Half- k -space EPI permits acquisition of an image in a shorter time than full- k -space acquisition by approximately a factor of $\frac{1}{2}$ for any desired matrix. The sequence also permits the echo time (TE) to be short since the center of k -space is collected first. At short TE, more lines of k -space can be acquired before signal intensity is lost due to T_2^* decay. Conversely, at short TEs, the BOLD percent enhancement is expected to decrease (7). This tradeoff is investigated here, extending the preliminary studies in Ref. 1.

Consideration of the y -axis point spread function (PSF) arising from T_2^* decay is of critical importance in high-resolution gradient-recalled single-shot EPI. The subject was discussed in Ref. 1, and that development is extended here. T_2^* decay is represented in Fig. 1a as a decaying exponential during acquisition of 128 lines of full k -space. For half k -space, T_2^* decays proceeds only over the acquisition of 64 lines of k -space, beginning at the center, and the other 64 lines are obtained by formation of the complex conjugate, as described in Ref. 1. Fig. 1a compares the weightings of the lines of k -space using half and full k -space acquisition. In Fig. 1b, the PSF for each of these acquisitions, assuming a T_2^* value of 40 ms, has been calculated using both a continuous Fourier transform (FT) of the curves of Fig. 1a following Eq. [4] of Ref. 1 (solid lines), and a discrete combined filter FT (solid circles) following the procedures of Refs. 8 and 9, which combine T_2^* decay and image acquisition. The differences are small, consistent with section 13.5.1 of Ref. 9.

The PSF is substantially narrower for half- than for full- k -space acquisition, which is a notable advantage for high-resolution EPI. Although it is customary to discuss PSFs in terms of the full (or half) width at half height, it is clear from Fig. 1b that use of a single number to characterize the PSF is inappropriate if line shapes vary. The discrete combined filter FT mimics the experiment, and a

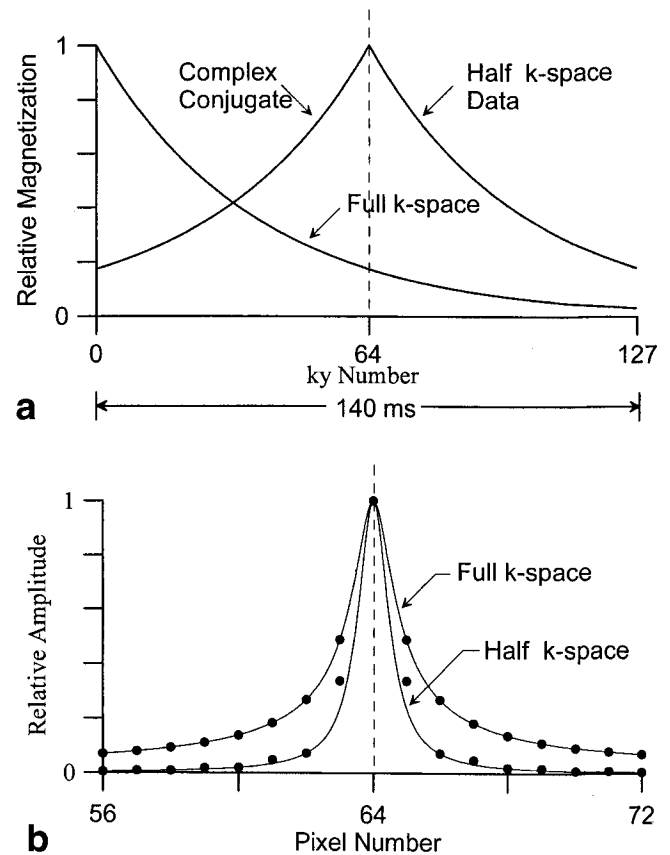


FIG. 1. **a:** Relative weightings of the lines in k -space for full- and half- k -space acquisition. **b:** Point spread functions for full- and half- k -space using continuous (lines) and discrete combined filter (dots) Fourier transforms (FTs) of the curves in **a**. Differences are small.

better characterization is provided by the signal intensities in the first and second nearest neighbor pixels assuming normalized intensity of the central pixel. In the case of Fig. 1, these values are for full k -space: 0.49 and 0.27, and for half k -space 0.34 and 0.07. Ratios of half- to full- k -space values for first and second nearest neighbors are 0.69 and 0.27, respectively.

Not only does the use of half k -space reduce image blurring, it also enhances intensity, since TE at the center of k -space is greatly reduced. For a single isolated voxel in real space as the signal source in the example of Fig. 1, the ratio of the intensities of the central pixel comparing half- and full- k -space acquisition is 5.75. Full- k -space acquisition would not be practical. Simulations of signal intensities for other clusters of voxels are shown in Fig. 2 of Ref. 1.

MODEL FOR FMRI CNR

The results presented here would not be possible based on the classic model of BOLD contrast of Menon et al. (7). These authors proposed a model of fMRI CNR given by Eq. [1]:

$$\frac{S(\text{fMRI})}{N} = \frac{S_0}{N_T} [e^{-(TE/T_2^*)} - e^{-(TE/T_2^*)}], \quad [1]$$

where T_2^* and $T_2^{*'}$ are T_2^* values in the absence and presence of activation and N_T is thermal noise of the scanner and is presumed to be white. S_0 is different for every pixel. It can be determined in several possible ways, including, for example, cross correlation of a pixel time course with a boxcar waveform (Eq. [2]).

$$S_0 = \boldsymbol{\sigma}_f \cdot \boldsymbol{\sigma}_r \quad [2]$$

where $\boldsymbol{\sigma}_f$ is a vector formed from the points in an experimental pixel time course and $\boldsymbol{\sigma}_r$ is a reference vector—for example, a boxcar waveform (10). In this example, N_T could be estimated similarly by cross correlation of a pixel time course that lies in free space and shows no evidence of ghosting, taking into account the numerical factor of 1.526 (11,12) that converts thermal noise in free space to thermal noise in the presence of signal.

$S(\text{fMRI})$ is zero at $\text{TE} = 0$ and at $\text{TE} = \infty$ with a maximum at $\text{TE} = T_2^*$. According to Eq. [1], use of short TE values, as employed in the present work, would severely impact the CNR. Moreover, a voxel size of 1 mm would also seem to penalize the CNR. If activated regions are large, the CNR would be expected, from Eq. [1], to vary inversely with the voxel volume. In fact, we have experimentally found that 1-mm³ voxels and short TE values can be used without apparent detriment. In order to resolve the discrepancy between Eq. [1] and the results presented here, we introduce a new model of fMRI CNR.

Weisskoff et al. (13) carried out analysis of the noise in pixel time courses from various regions of resting brain by Fourier transformation to the frequency domain of data obtained using a TR value that was short enough to avoid aliasing of the cardiac rate. They observed cardiac and respiratory peaks of various magnitudes in various brain regions. In addition, they discovered intense low-frequency noise in gray matter. The work of these authors casts doubt upon the validity of the noise treatment in Eq. [1].

Biswal et al. (14–16) showed that these low-frequency fluctuations, or at least some portion of them, arise from fluctuations in blood oxygenation through a spontaneous BOLD mechanism. The hypothesis tested in their studies was that spontaneous and task-induced neuronal events each result in modulation of blood oxygenation through identical physiological processes. The literature of physiological fluctuations in fMRI has been reviewed by Hyde and Biswal (17).

On the basis of this literature, the model of Eq. [3] for fMRI CNR is introduced:

$$\frac{S(\text{fMRI})}{N} = S_0 \frac{[e^{-(\text{TE}/T_2^{*'})} - e^{-(\text{TE}/T_2^*)}]}{\langle \{N_B [e^{-(\text{TE}/T_2^{*'})} - e^{-(\text{TE}/T_2^*)}] + N_O + N_T + N_{SC}\}^2 \rangle^{1/2}}, \quad [3]$$

where N_B , N_O , N_T , and N_{SC} stand, respectively, for physiological noise of BOLD origin, other physiological noise, thermal noise, and scanner noise arising from system instabilities.

The four noise terms in Eq. [3] are functions of time, and N_B , N_O , and possibly N_{SC} are pixel-wise dependent. Brackets in the denominator of Eq. [3] denote time-course averaging, noting that all of these various sources of noise may not be independent. Since the noise is structured, analysis of Eq. [3] must be carried out in the frequency domain. For example, a boxcar reference vector $\boldsymbol{\sigma}_r$ has components at the first, third, and fifth harmonics of the repetition frequency. Because of the spectral dependence of physiological noise, the noise at these various harmonics progressively decreases as the harmonic number increases, and also as the epoch duration decreases. This model predicts that if the N_B term dominates other noise terms, $S(\text{fMRI})/N$ is independent of TE. It also predicts that in the absence of partial voluming of the activated volume, the CNR should be independent of voxel volume. In addition, the noise should be proportional to the percent enhancement for all activated voxels, which leads to the observation that even though the noise varies from pixel to pixel, the CNR should be constant from pixel to pixel.

A qualitative discussion of Eq. [3] can be developed by assuming an ideal boxcar signal in a particular pixel time course to which noise has been added. The two states of the boxcar response correspond to T_2^* and $T_2^{*'}$ in the numerator of Eq. [3]. The noise is described by the denominator of Eq. [3], although a legitimate question concerns the appropriateness of a two-state model for the N_B term. The FT of the noise results in a term at the first harmonic frequency of some unknown phase. The two signals at the first harmonic frequency in the time domain, task response, and noise add vectorially. The effect of the noise is to shift the phase and amplitude of the resultant first harmonic signal relative to that of the pure task-induced signal. This analysis is readily extended to include other harmonics present in the ideal task response, primarily the third and fifth.

The two-state model for the N_B term characterized by T_2^* and $T_2^{*'}$ should, we suspect, be elaborated to allow for a time-varying distribution of T_2^* values. Thus Eq. [3] is amenable to further refinement. One conceptual approach to measurement of the N_B term would be to perform multiple intrasubject, test-retest, task-induced fMRI experiments, and measure the standard deviation (SD) of the response at each activated pixel. Another approach would be to collect separate resting-state data that are well registered in space with task-activation data. Still another possible approach is to estimate the noise in a task-induced data set at the first harmonic frequency by extrapolation in the frequency domain of noise levels at other frequencies. We present here a variety of experiments to test Eq. [3].

Preliminary reports of aspects of this work have been presented in abstract form (18–21). A preliminary discussion of Eq. [3] appears in Ref. 17.

METHODS

General

All studies were performed on a 3T BIOSPEC 30/60 Bruker scanner (Bruker Medizintechnik GMBH, Karlsruhe, Germany), using a local gradient coil and RF coil specifically designed for optimum performance in EPI of the human brain. Additional technical details are given in Ref. 1.

Informed consent was obtained from all subjects, and all protocols were IRB approved. The field switching rates did not exceed 20 T/s. Acoustic noise levels were under FDA limits (22).

As resolution increases, subpixel registration of the images in a time course becomes increasingly critical. Registration was carried out within the AFNI software framework (23–25). The algorithm is based on a four-way 3D shear matrix factorization of the rotation matrix (26), and employs Fourier interpolation in the resampling process.

A multiplanar gradient-recalled (MPGR) sequence was used to produce a 3D map of the field in the head of each subject (26). This map is decomposed to 14 shimming polynomials that are calculated from the actual windings of the shim coils. The entire shimming procedure takes 90 s, including image acquisition, computation, and loading of shim-current values. The advantage of the technique is that higher-order polynomials, including $Z(X^2 - Y^2)$ and Z^2XY , are set on the basis of rigorous analysis. Setting them manually was found to be difficult.

Partial *k*-Space GR-EPI

The details of reconstruction are described in Ref. 1, and the methodology employed in the present study is similar in most details to that described in Ref. 1, although extended to multislice acquisition using a water-cooled gradient coil. Most data were acquired in axial slices through the motor cortex near the top of the head using a field of view (FOV) of $12.8 \times 12.8 \text{ cm}^2$ and a matrix size of 128×128 . The bandwidth was set at 166 kHz. The FOV and matrix used here minimize the effect of T_2^* decay during acquisition. The acquisition time was 70 ms, and the effective acquisition window (*eaw*, see Ref. 1) was 140 ms, resulting in a *y*-axis point spread function of 1.1 mm for a T_2^* value of 40 ms. The task-activation paradigm was self-paced bilateral finger tapping.

The partial *k*-space pulse sequence of Ref. 1 has been modified to permit (for a given set of experimental parameters, including TE) as many overscan lines as permissible with the proviso that the number of such lines be an even number. Overscan lines are used to produce a phase map in order to center the central echo. This modification permits formation of the best possible phase map for a given TE value.

Image Processing

For most of the studies reported here, the AFNI software framework was used (23–25). An idealized boxcar reference waveform representing the “on/off” cycle was used as a reference for cross-correlation with every pixel in the brain on a pixel by pixel basis, following Ref. 10. The option to adjust the reference phase automatically for each pixel time course over a preset range of hemodynamic delays was used in most studies. All pixels with correlation coefficient (CC) greater than a fixed threshold were considered active and belonging to the sensorimotor and its associated cortices. Task-activation percent signal changes were calculated relative to baseline values. These values were also calculated for the corresponding pixels from resting-state scans.

RESULTS AND DISCUSSION

Protocol 1. The Thick Slice/Thin Slice Task-Activation Experiment

In this protocol, a bilateral self-paced finger-tapping paradigm (TR = 2 s, 60 s rest followed by three epochs of 40 s on/40 s off) was used. The in-plane matrix was 128×128 over an FOV of $12.8 \times 12.8 \text{ cm}^2$. Data were first acquired using a 1-cm-thick slab, followed by acquisition of data from 10 contiguous slices 1 mm thick from the same region. TE = 30 ms. Seven subjects were scanned. Each task-activation acquisition was accompanied by a matching acquisition of resting-state data. Data presented here are from a single subject.

Figure 2a shows a display of pixel time courses from the motor cortex in a 9×9 array obtained from a slab of tissue $9 \times 9 \times 1 \text{ mm}^3$ using cubic 1-mm voxels. The three task-activation epochs are readily apparent in many of the time courses. Spatial variability on a distance scale of the order of 1 mm is apparent. This figure provides visual evidence that partial volume effects must be present in data acquired using larger voxels. Similar data were acquired from all subjects in the study. It is concluded that use of 1-mm^3 voxels obtained using half-*k*-space GR-EPI is practical.

Figure 2b was constructed from resting-state data obtained immediately after acquisition of the data of Fig. 2a. The display is the magnitude of the FT of the resting-state time courses carefully registered with Fig. 2a. The term at zero frequency, i.e., the mean value, was deleted. It is immediately evident that each voxel that results in a readily apparent three-epoch time course in the task-activation data of Fig. 2a also gives rise to an intense low-frequency peak in the resting-state frequency-domain display of Fig. 2b. The intense low-frequency noise, which overlaps with the frequencies of the first and third harmonics of the task-activation paradigm, is the limiting noise source. It follows, because the noise is colored, that an estimate of the signal-to-noise ratio (SNR) in the time-domain display of Fig. 2a is unreliable. Figure 2 provides the rationale for this study: 1) good task-activation data can be obtained using 1-mm^3 voxels, 2) low-frequency physiological fluctuations are the limiting noise source, and 3) partial volume effects must be considered in fMRI experiments.

Figure 3a shows a histogram of percent enhancements for all voxel time courses in the 1-cm-thick slice that have a CC with a boxcar reference waveform greater than 0.5. There are 563 such needle-shaped $1 \times 1 \times 10 \text{ mm}^3$ voxels. A mask defined by 0.5 CC in the thick-slice experiment was used to define regions of interest (ROIs) in the corresponding 10 thin slices. Thus, there are 5630 thin-slice $1 \times 1 \times 1 \text{ mm}^3$ voxels of interest. Figure 3b is a histogram of percent enhancement for the time courses of cubic voxels within the mask that had a CC above 0.5. There are 182 such voxels. Figure 3c is similar to 3b, but the CC was lowered to 0.25. Of the possible 5630 voxels, 2203 pass this threshold. Figure 3d is a histogram of percent enhancements of time courses from all 5630 voxels that lie within the mask. Many voxels at low percent enhancement show little or no activity. These are ascribed to inactive tissue that was partial volumed into

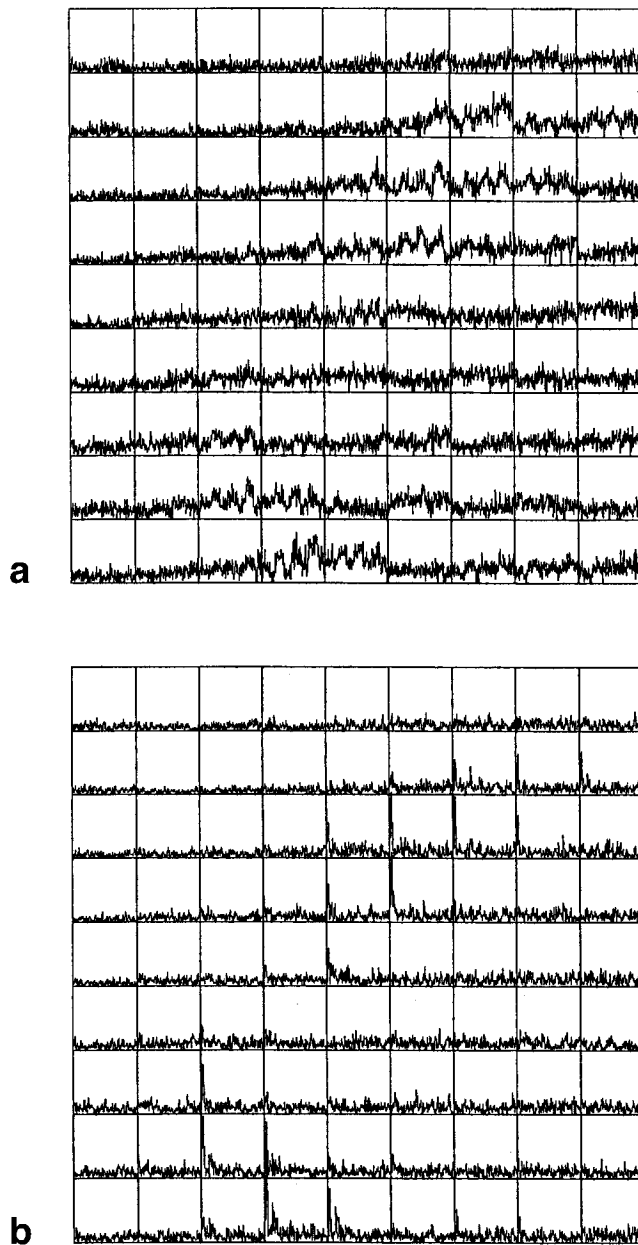


FIG. 2. **a**: Pixel time courses in a bilateral finger-tapping task 9×9 pixel array from 1-mm^3 voxels. Half- k -space GR-EPI, TE = 30 ms, 3T. The CNR is good in spite of the small voxel size. **b**: 9×9 array of FT magnitudes of resting-state pixel time courses aligned precisely with **a**. Intense low-frequency peaks are observed in voxels that also respond to task activation.

the mask in Fig. 3a. Figure 3e was formed by adding all fMRI pixel time courses in each column of data in the 10 thin slices to simulate the needle-shaped voxels in the thick-slice experiment of Fig. 3a. Histograms 3a and 3e are very similar. Thus, the addition of pixel time courses using high-resolution data to mimic low-resolution data results in data that are about the same as actual acquisition of the low-resolution data. This spatial linearity is the expected result when BOLD signal response, baseline, and noise are each spatially encoded.

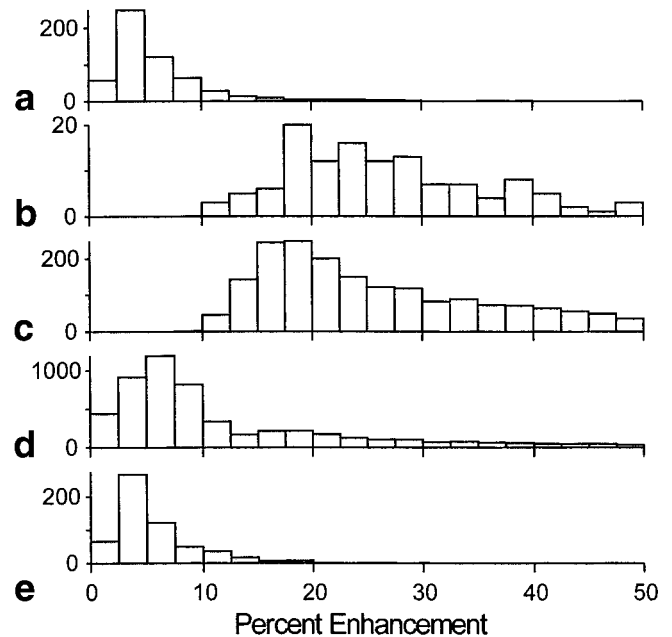


FIG. 3. Histograms of percent enhancement in the motor cortex: **(a)** thick-slice ($1 \times 1 \times 10\text{ mm}^3$ voxels) and **(b–e)** thin-slice data ($1 \times 1 \times 1\text{ mm}^3$) using 10 contiguous 1-mm-thick slices from the same region as **a**. See text for details.

Figure 4 is based on the thick-slice mask defined by Fig. 3a. For each voxel in the thin-slice data that lies within the mask, the percent enhancement and cross-CC were determined, and the point was entered on the scatter plot of percent enhancement vs. CC, as shown in Fig. 4. There is a general correlation of these parameters—the higher the CC the more likely that the percent enhancement will also be higher.

Protocol 2. Test of Eq. [3]: Spatially Registered Task-Activation and Resting-State Time Courses

This protocol closely follows Protocol 1 (i.e., 10 contiguous 1-mm slices with $1 \times 1\text{ mm}^2$ in-plane pixel size). The finger-tapping timing was 30 s rest, three epochs of 20 s on/20 s off, and 60 s rest, with eight subjects. Each data set consisted of a task-activation acquisition followed by a

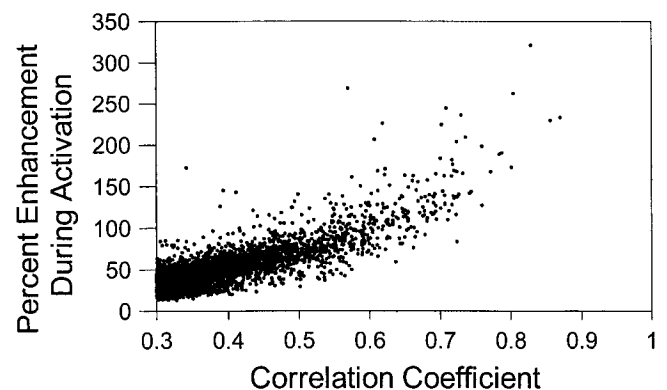


FIG. 4. Scatter plot of percent enhancement vs. correlation coefficient (CC) for the voxels defined by Fig. 3d.

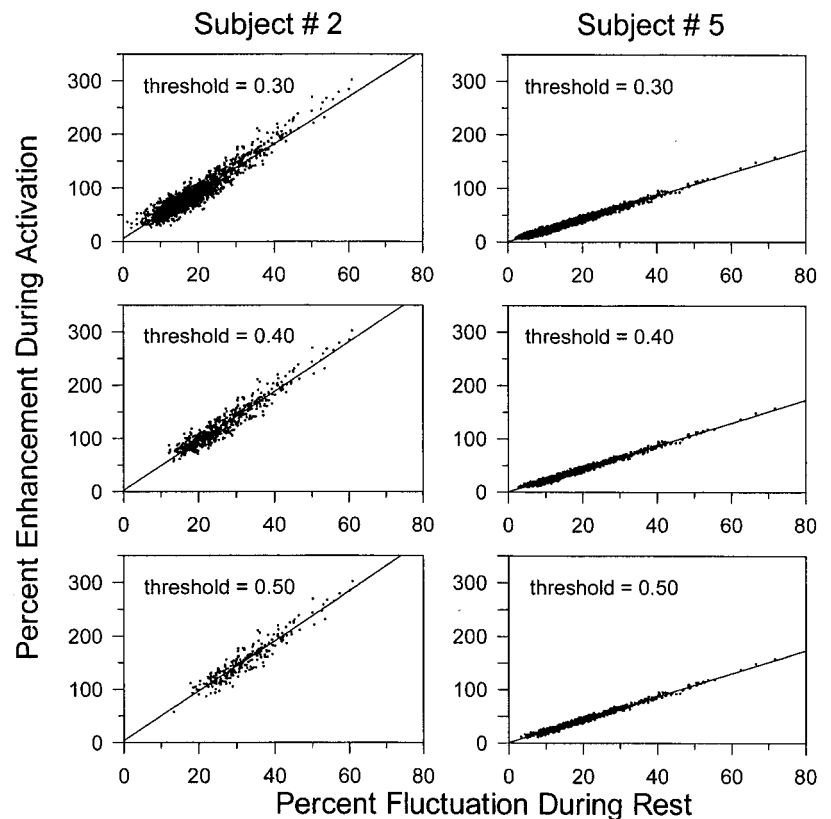


FIG. 5. Scatter plots formed from percent enhancement during activation and percent fluctuation during rest for activated pixels that pass 0.3-, 0.4-, and 0.5-CC thresholds.

resting-state acquisition taken with almost no delay to avoid misregistration. Matched data sets were obtained at TE = 20 and 40 ms. Resting-state time courses were passed through a low-pass filter cutting off at 0.1 s. The resulting noise was estimated for each pixel in the time domain by calculating the SD divided by the mean value in that pixel, expressed as a percent. SD and mean values were also tabulated separately. Task-activation time courses were analyzed by cross-correlation with a boxcar reference vector (10). For each pixel the delay was automatically varied over a range of 0–16 s for maximum CC.

Scatter plots of percent enhancement during activation vs. percent fluctuation during rest are shown in Fig. 5 for two of the subjects, for a TE value of 40 ms. Percent task-activation enhancements were calculated for each pixel by dividing by the baseline value. The mean value of

the resting-state time course in a given pixel time course, assuming ideal data, equals the baseline value in the task-activation time course from that pixel. Thus, both the ordinate and the abscissa in Fig. 5 are ratios that have, in principle, the same denominator for each data point. The numerators are expressed in self-consistent units, leading to the conclusion that the task response in a given voxel is three to five times greater than the SD about the mean value of the low-frequency physiological fluctuations. Similar data were obtained at TE = 20 ms, and results across subjects were also similar. It is apparent from Fig. 5 that the data for percent enhancement and for percent fluctuation are linearly correlated. The data can be fitted to a linear model, $y = ax + b$, where b is the intercept on the vertical (y) axis. Slopes, x -axis intercepts, and linear regression coefficients (R^2) are summarized in Table 1. Re-

Table 1
Parameters for the Equation $y = ax + b$ for Data as Shown in Fig. 4

Subject	CC = 0.3			CC = 0.4			CC = 0.5		
	a	b	R^2	a	b	R^2	a	b	R^2
1 ^a	2.83	7.43	0.97	2.87	9.45	0.98	2.84	9.87	0.99
2	4.40	5.60	0.89	4.64	2.40	0.91	4.68	3.60	0.89
3	2.07	-3.67	0.96	2.10	-4.14	0.97	2.16	-5.47	0.98
4	3.51	4.89	0.89	3.52	7.95	0.91	3.52	6.79	0.93
5	2.14	0.69	0.98	2.15	0.61	0.98	2.15	0.69	0.98
6	3.87	-16.86	0.97	3.93	-17.90	0.99	3.95	-18.74	0.99
7	3.49	-31.09	0.95	3.52	-38.42	0.96	3.53	-42.65	0.97
8A	3.21	-8.30	0.92	3.11	-7.30	0.91	3.06	-7.90	0.90
8B	2.84	-15.30	0.84	2.96	-16.10	0.88	3.06	-16.90	0.91

^aTE = 40 ms for Subjects 1–7 and 8A, 20 ms for 8B.

gression coefficients are high across all subjects, and do not depend on the CC threshold used for selection of pixels. Small differences in slopes and intercepts occur depending on whether percent enhancement or percent fluctuation is considered to be the dependent variable in the fit. Interpretation of the meaning of the intercept may not be warranted, although the contribution of thermal noise to the total noise level according to the denominator of Eq. [3] is expected to shift the x -axis intercept to higher values. The slopes (term a , reported in Table 1) are independent of TE, also as predicted by Eq. [3]. There is considerable variation of the slope, which is the CNR, across subjects: 3.2 ± 0.6 . Subject 2 exhibited the highest task activation response and the largest slope. The R^2 values for subject 5 data are 0.98 for all three CCs. Overall, Fig. 5 and the data of Table 1 demonstrate the validity of the model of Eq. [3].

The use of cubic-millimeter voxels would be expected to make the results of the study more sensitive to motion. Motion correlated with the task would be expected to affect the placement of a data point on the ordinate of Fig. 5. Likewise, motion during rest would affect placement on the abscissa. Thus, motional effects should adversely affect the linear regression coefficients (Table 1).

Every point at a threshold of 0.50 appears in the scatter plots at thresholds of 0.40 and 0.30. Similarly, every point at a threshold of 0.40 appears in the scatter plot at a threshold value of 0.30. As is apparent in Fig. 5, the numbers of high percentage points above about 35% fluctuation during rest are independent of the threshold; all have high CCs with a boxcar reference. The BOLD responses to task-activated neuronal activity and to spontaneous neuronal activity are each governed by the hemodynamic response function, and thus they both tend to have the same harmonic content in the frequency domain. This is the rationale for Eq. [3] and for the design of Protocol 2. However, the task-activation paradigm can be designed with an arbitrary time course, and it is possible that some paradigms, including event-related paradigms, will be advantageous in the presence of spontaneous BOLD fluctuations.

Figure 6a shows a histogram of mean (baseline) values from the resting-state data used to produce the 0.4 threshold scatter plot from subject 5 (Fig. 5). We had expected that activated voxels would primarily lie in gray matter with uniform brightness and a relatively narrow distribution of mean values. Fig. 6a shows that this is not the case. In spite of the great variability of baseline values resulting in a corresponding large range of percent enhancement and percent fluctuation during rest, all points in the scatter plot of Fig. 5 exhibit the linear dependence predicted by Eq. [3].

Figure 6b is a scatter plot extracted from the ratios of SD divided by mean value that were used to calculate the percent fluctuations during rest for Fig. 5, subject 5, threshold 0.40: numerator values (SD) vs. denominator values (mean values of the signal intensity, i.e., baseline values). Brighter voxels generally exhibit larger amplitudes of low-frequency fluctuations. The fact that the raw data going into the construction of Fig. 5 is so complex, as illustrated by Fig. 6, and that nevertheless the resulting

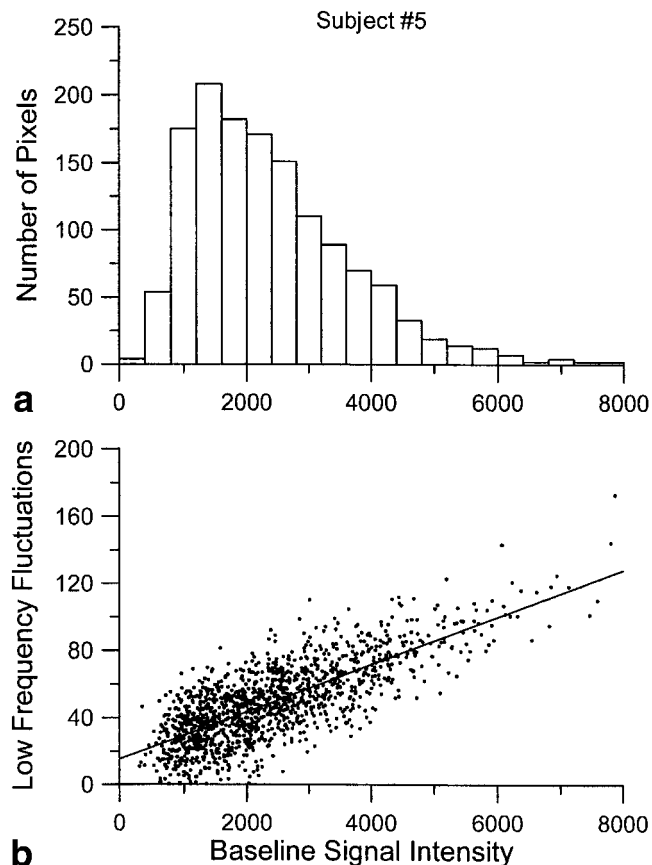


FIG. 6. **a:** Histogram of mean values of the filtered resting-state time courses from the data used to produce Fig. 5, subject 5, threshold 0.4. These are the values for the denominator that were used to calculate percent fluctuation at rest in that display. **b:** Scatter plot of the SD of low-frequency fluctuations vs. baseline mean values, i.e., numerator vs. denominator of percent fluctuations at rest used in Fig. 5, subject 5, threshold 0.4. A best-fit linear model is superimposed.

plots of Fig. 5 have R^2 values close to unity is interpreted as further support for Eq. [3].

Figures 7 and 8a present data which test the prediction of Eq. [3] that the CNR is independent of TE value within a certain range. The data are from subject 5 (see Fig. 5). Figure 7 is a scatter plot of task-activation CC at TE = 40 ms vs. task-activation CC at TE = 20 ms for all pixels that exhibit a task-activation CC above 0.4. In this particular data set, a negligible number of pixels pass the 0.4 threshold at one TE value but not at the other. Fig. 7 shows that task-activation experiments at 20- and 40-ms TE values result in data of equivalent quality, as predicted by Eq. [3]. Figure 8a shows histograms of CCs at TE values of 20 and 40 ms. These displays provide additional statistical evidence that task-activation experiments at 20- and 40-ms values result in equivalent data. In other experiments currently in progress, data obtained at 10-, 20-, 30-, and 40-ms TE values were found to be substantially equivalent.

Fig. 5 compares task-activation with low-frequency noise on a pixel-wise basis, while Figs. 7 and 8a analyze task-activation responses at two TE values on a pixel-wise

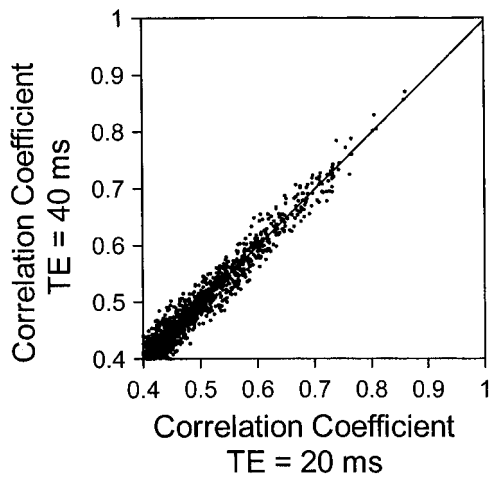


FIG. 7. Scatter plot of CCs in activated pixels for TE values of 20 and 40 ms.

basis without explicit consideration of noise. Similar results have now been obtained across 10 subjects with varying technical parameters.

Figure 8b shows histograms of percent enhancement at TE values of 20 and 40 ms. The theory of fMRI contrast of Menon et al. (7) predicts that the percent enhancement should vary with TE value according to Eq. [4].

$$\frac{\Delta S}{S} = e^{-TE[(T_2^*)^{-1} - (T_2^*)^{-1}]} - 1 \quad [4]$$

See Eq. [1], above, for definitions of terms. The expression in square brackets is negative, and $\Delta S/S$ therefore increases linearly with TE at low TE values, and exponentially at higher values. The mean value of all percent enhancements in Fig. 8b is expected, according to Eq. [4], to double as TE increases from 20 to 40 ms. In fact, the increase is 23%. Analysis across the eight subjects in Protocol 2 yields an average increase in mean percent enhancement of $23 \pm 12\%$. Since Menon et al. (7) present experimental data supporting Eq. [4], a conundrum arises. It is apparent that water protons in brain experience a heterogeneity of T_2^* values (27), and we hypothesize that

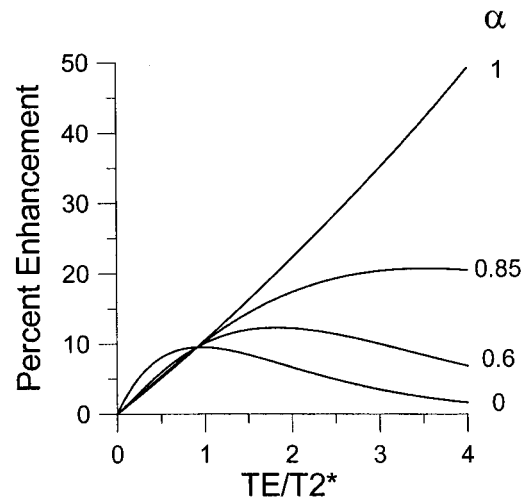


FIG. 9. Plot of Eq. [5] for selected values of the parameter α . T_2^* was assumed to differ from T_2^* by 10%.

the weak dependence of percent enhancement is a consequence of this heterogeneity. A stretched exponential is sometimes used in the MR literature as a convenient analytical approximation to a sum over an unknown distribution of exponential decays (28,29). Equation [4] then becomes

$$\frac{\Delta S}{S} = \frac{S_1(e^{-TE/T_2^{*'}} - e^{-TE/T_2^*})}{S_0 e^{-(TE/T_2^*)^\alpha}} \quad [5]$$

where $0 < \alpha < 1$ and S_1/S_0 is the fraction of water protons in an activated voxel that contribute to the BOLD signal. This equation is plotted in Fig. 9 for several values of α . When $\alpha = 0$, Eq. [5] has the form of Eq. [1], and when $\alpha = 1$, of Eq. [4]. Values in the range of 0.6–0.85 appear consistent with the data available in Protocol 2. Experiments over a wide range of TE values at high SNR are required to provide a more definitive test of Eq. [5]. The percent enhancement has also been determined for each pixel in the data of Fig. 8b that passes the threshold for both TE values. Substantial variance was found indicating, within the

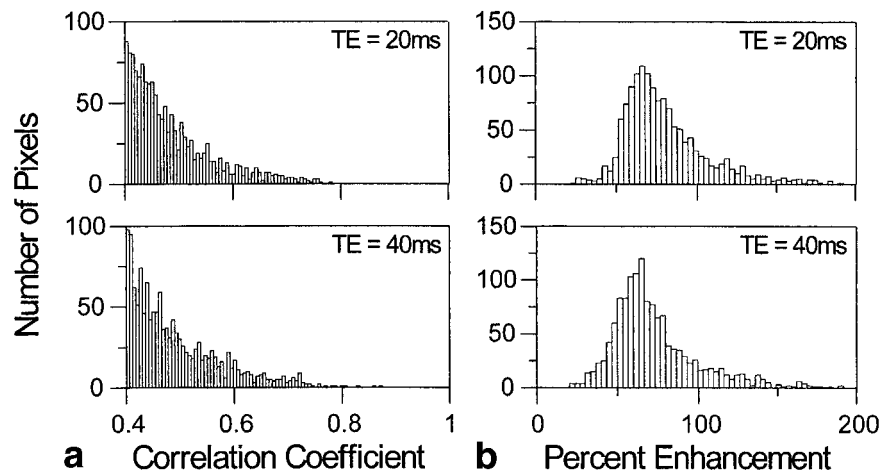


FIG. 8. **a**: Histogram of CCs for pixels with CC above 0.4. **b**: Histogram of percent enhancement for the pixels of **a**.

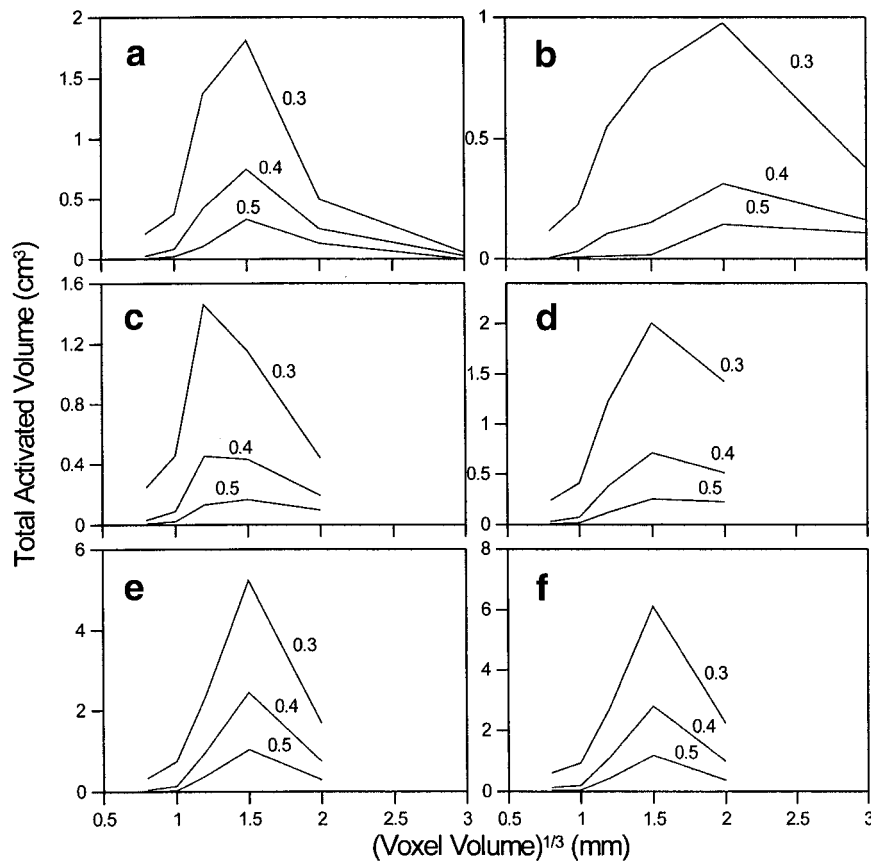


FIG. 10. **a-f**: Data demonstrating that use of 1.5-mm cubic voxels is optimum in fMRI (six subjects).

model of Eq. [5], considerable variation of intravoxel T_2^* heterogeneity across voxels.

Equations [1] and [3]–[5] are based not only on the assumption that T_2^* exhibits no intra- or intervoxel heterogeneity, but also on the assumption that all lines of k -space are acquired at the same TE. In GR-EPI, the latter assumption is violated, although half- k -space acquisition beginning at the center of k -space has less variation than full k -space (see Fig. 1). Nonuniform weighting of the lines of k -space during acquisition can contribute to the differences observed experimentally and in the models of Eqs. [1] and [4].

Protocol 3. Optimum Voxel Size

This protocol addresses the question of whether the use of 1-mm³ voxels is in fact optimum, and, indeed, if an optimum voxel size exists. As for Protocols 1 and 2, the task was self-paced bilateral finger tapping and single-shot half- k -space GR-EPI was used (1). A scout data set of 10 contiguous 1-mm axial slices with 1 × 1 mm in-plane resolution was obtained through the motor cortex. From this data, using real-time analysis methods (26,30), an optimum 6-mm-thick slab was identified by the criterion of greatest volume of activation. This slab was sampled in six different ways in six separately acquired data sets: seven, six, five, four, three, and two slices (viz., .86-, 1-, 1.2-, 1.5-, 2-, and 3-mm slice thickness). The in-plane matrix size was held fixed at 192 × 192, and the FOV varied in each case to achieve cubic voxels of volume d^3 . The bandwidth remained fixed at 166 kHz. In this manner,

the thermal noise level in every pixel was held constant. Since physiological noise rather than thermal noise is dominant, the low-resolution data are not penalized by the use of a bandwidth that is greater than necessary. The order of acquisition of the six data sets was randomized. For each of the data sets, the number of activated pixels was determined as a function of the correlation-coefficient threshold. For each pixel time course, the delay of the boxcar reference waveform was adjusted for maximum response. Multiplication of the number of activated pixels by voxel volume yielded the total activated volume as a function of threshold. Data from the six sets were merged by plotting total activated volume vs. the parameter d for various threshold values. Image acquisition technical parameters were: TE = 30 ms, bandwidth = 166 kHz, 16 partial k -space overscan lines, TR = 2 s, and four cycles of 32 s on/32 s off.

Figure 10 shows individual results from six subjects. Note that the 3-mm slice thickness data set was added to the protocol midway in the study (subjects a and b). An optimum was observed at $d = 1.5$ mm in four subjects, 1.2 in one, and 2.0 in one. It is concluded that fMRI experiments ought to be carried out using 1.5 × 1.5 × 1.5 mm³ cubic voxels, although for some studies smaller values of d may be preferable because of partial voluming of the functional parameters of interest. At 1.5-mm resolution, the option exists of reducing the area of activation by increasing the threshold value. This would increase the significance of activated voxels.

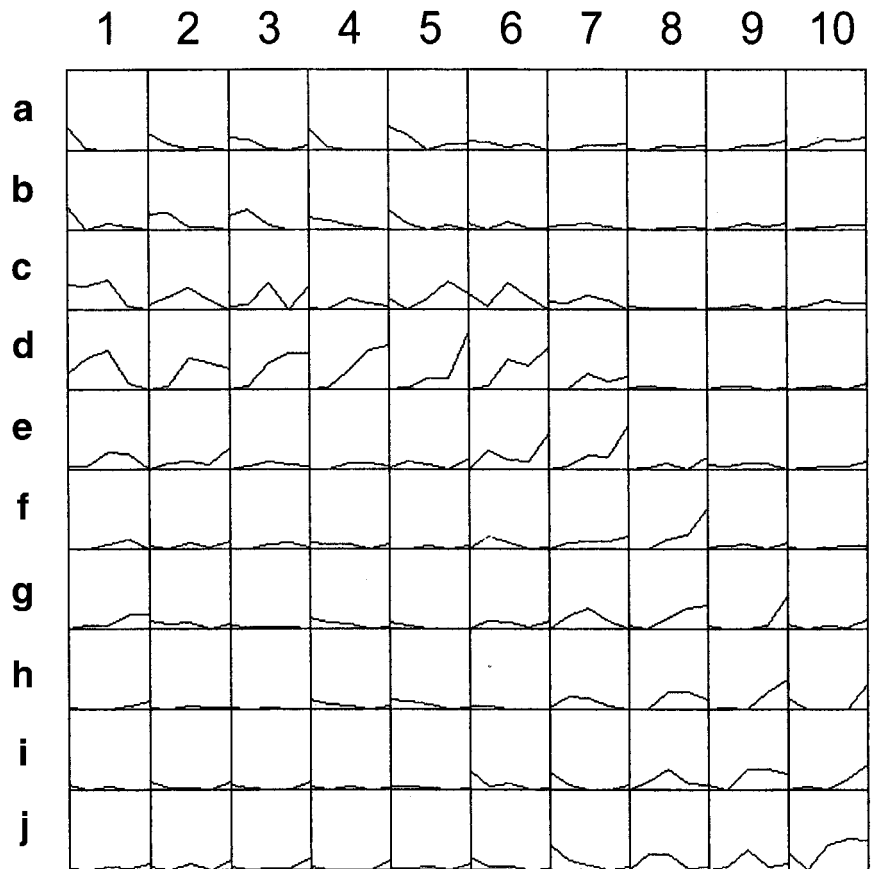


FIG. 11. Novel 3D display of task activation CCs from 1.2-mm cubic voxels in a slab of tissue in the motor cortex region $12 \times 12 \times 6 \text{ mm}^3$. See text for details. The figure illustrates several types of spatial organization that would result in different partial volume effects if larger voxels were used.

The existence of maxima in the plots of Fig. 10 can be rationalized in a qualitative manner. Assume an fMRI volume V_0 of uniform activation. If voxels are smaller than V_0 , the signal in a voxel that lies within V_0 varies as d^3 . If thermal noise dominates, as would be expected at sufficiently small voxel size, the noise is independent of voxel volume and the CNR therefore would vary as d^3 . However, Eq. [3] predicts that physiological noise arises from volume V_0 . As it becomes dominant with increase in voxel size, the CNR becomes independent of V_0 . As the voxel size progressively increases beyond V_0 , the signal remains unchanged, but inclusion of other tissue, including unactivated gray matter, results in increased noise and decreased CNR. The total volume of activated tissue (i.e., voxel volume times the number of voxels above a set threshold) can be expected to track the CNR values as the voxel size increases, resulting in the optima seen in Fig. 10. If the data of Fig. 10 were plotted as a function of voxel volume, d^3 , the observed optima would be quite broad, consistent with the prediction of Eq. [3] that the CNR tends to be independent of voxel volume in the absence of partial voluming of activated tissue. In the real case, with a distribution of activation levels, physiological noise levels, spatial correlation of noise, and irregular activation volumes, the situation is much more complex. Nevertheless, a maximum in the plots of Fig. 10 is expected when d^3 matches V_0 . The optimum values seen in Fig. 10 are consistent with the range of volumes assigned by Duvernoy et al. (2) to the venous unit.

Figure 11 is a display of 3D spatial information. The data used to produce Fig. 10c and Fig. 11 are from the same experiment. The array of squares corresponds to a 10×10 array of voxels in tissue, each $1.2 \times 1.2 \text{ mm}^2$ in the *en face* plane. The value of the CC in five contiguous slices, each 1.2 mm thick, is plotted left to right within each square. The vertical axis scale is the CC varying from 0 to 1 within each square. Thus, this is a display of all CCs in all voxels within a slab of tissue $12 \times 12 \times 6 \text{ mm}^3$ at a spatial resolution of $1.2 \times 1.2 \times 1.2 \text{ mm}^3$. The display gives insight into the nature of the spatial distribution of activated voxels in fMRI. Several features are apparent: 1) The intensity of voxels c1–3 and d1–4 is high and nearly uniform in the central slice. 2) Voxel c3 shows two well-defined peaks separated by a voxel of nearly zero intensity. 3) Voxels d5, e6, and 7, and f8 in slice 5 exhibit very high CC values that could arise from a pial vein. 4) Voxels d2–6 suggest a ribbon of tissue a few voxels wide perpendicular to the plane of the page. The central points of Fig. 11 are the complexity of the spatial patterns of activation, the observation that the CC threshold may cut off information that appears significant based on the spatial pattern, and that partial voluming of fMRI data occurs quite generally whenever larger voxels are used.

CONCLUSIONS

The hypothesis that the limit of fMRI spatial resolution based on BOLD contrast is determined by the anatomy of

the microcirculation is supported by the studies presented in this work. Specifically, that limit in cortex appears to be the venous unit defined by Duvernoy et al. (2): the veins that penetrate gray matter and are fed by branching veins that reach out into vascular layer 3, together with the arterial ring or rings that surround each of these penetrating veins. This hypothesis should, however, be tested more extensively.

Detectable BOLD signals that are secondary to neuronal activity are divided here into two categories: those that are in response to an external cue and those that are a consequence of a spontaneous internal neuronal event. Task response is in synchrony with external cues, spontaneous neuronal activity is asynchronous. If task response is the signal of interest, then asynchronous BOLD signals are in fact noise. This verbal expression of fMRI CNR is quantified by Eq. [3]. This equation is supported by the studies reported here: 1) The task response in a given pixel is proportional to the low-frequency resting-state physiological fluctuations in that pixel; 2) fMRI CNR data acquired using GR-EPI are insensitive to the choice of TE values. Values in the range of 15–20 ms can be used at 3T without loss of image quality. 3) Equation [3] predicts that at sufficiently low fMRI response, thermal noise should replace physiological noise as the dominant noise source. This predicted effect has not been observed definitely, although intercepts shown in Table 1 obtained using 1-mm cubic voxels suggest the presence of thermal noise. Voxels of this size are practical.

It has been discovered that voxels of $1.5 \times 1.5 \times 1.5 \text{ mm}^3$ yield optimally robust fMRI task-induced response in the motor cortex at 3T. The existence of an optimum voxel of this size is consistent with partial voluming of the venous unit, but more needs to be learned about spatial correlation of physiological noise to make a testable model for the observed optimum voxel size.

Various issues of linearity of fMRI response arose in this study. If a voxel is divided into subvoxels, the signals including noise from the subvoxels can be added to produce the signal and noise of the voxel itself (Fig. 3a compared with Fig. 3e). This follows because both the signal and the noise are spatially encoded. The hemodynamic delays of the subvoxels add up to produce the hemodynamic delay of the voxel. This linearity is expected if thermal noise is not dominant and there are no problems of local susceptibility variation giving rise to intravoxel dephasing. A potential nonlinearity issue is whether physiological noise is the same in the presence of task activation as it is during rest, although data presented here indicate that attention to task does not strongly affect the level of underlying physiological fluctuations. This is an important neuroscience issue that requires further investigation.

Percent enhancement values reported here using small cubic voxels are much higher than those reported by others. This may partly be a consequence of minimizing partial volume effects by matching the size of the voxel to the size of the signal source, but it can also be a straightforward consequence of reduced baseline signal intensity because of the small voxel size. The dependence of the percent enhancement on TE value was weaker than predicted by the theory of Menon et al. (7). An alternative

model based on the assumption that baseline signal arises from a heterogeneity of local water proton environments, each with its own T_2^* value, was developed. The composite T_2^* relaxation was characterized by a stretched exponential. This model was found to be consistent with the limited amount of data that has been acquired thus far.

In the frequency domain, physiological fluctuations tend to increase as the frequency decreases (as shown in Fig. 2b). Thus, there can be considerable advantage to the use of tasks that have, in the frequency domain, harmonic content at the highest possible frequencies. This can be true even if there is some loss of response at high frequencies because of the sluggish hemodynamic response.

In summary, it has been established that underlying BOLD fluctuations should be considered in the design of fMRI paradigms. We have concluded that cubic voxels are desirable, that use of half- k -space acquisition is generally desirable when using a GR-EPI sequence for high-resolution fMRI, and that $1.5 \times 1.5 \times 1.5 \text{ mm}^3$ is a reasonable default voxel size in fMRI. Although we believe that the results of this study are applicable to other brain regions, and have some preliminary data in support of this belief, further studies are appropriate.

It is still not possible to obtain whole-brain data at optimum resolution in a single shot. A detailed estimate of the maximum number of slices that can be obtained using our hardware with TR = 2 s, an FOV of $19.2 \times 19.2 \text{ cm}$, a matrix of 128×128 , and a single-shot half- k -space sequence, within FDA guidelines is 25 (80 ms per image with TE = 15 ms), corresponding to 3.75 cm for cubic voxels 1.5 mm on an edge. A practical strategy for sagittal or coronal acquisitions, which we have implemented, is to obtain a scout data set over the entire brain and to use it to place two symmetric bilateral slabs of contiguous high-resolution slices in ROIs.

This work permits speculation about the limits of spatial resolution in fMRI at higher static field strengths. Both contrast and noise increase relative to thermal noise, NT (Eq. [3]), permitting the use of smaller voxels without degrading the CNR. Higher field strength can be expected to lead to improved resolution at constant CNR, but not to higher CNR at constant resolution. There are at least two deleterious trends as the field strength increases: T_1 increases, reducing the overall rate of data collection, and T_2^* decreases, reducing the number of lines of data that can be acquired in a single shot. Thus, the rationale for half- k -space acquisition increases as the field increases. Animal fMRI studies will be enhanced because human limits on dB/dt do not apply. However, interleaved partial- k -space EPI may well be necessary for high-resolution fMRI in humans at high-field strength.

ACKNOWLEDGMENTS

This work was supported by grants MH51358 and CA41464 from the National Institutes of Health. Additional resources for this work were made available through NIH grant M01 RR00008-GCRC. The authors have benefited from numerous discussions with their colleagues R.W. Cox and B.D. Ward.

REFERENCES

1. Jesmanowicz A, Bandettini PA, Hyde JS. Single-shot half k-space high resolution gradient recalled EPI for fMRI at 3 Tesla. *Magn Reson Med* 1998;40:754–762.
2. Duvernoy HM, Delon S, Vannson JL. Cortical blood vessels of the human brain. *Brain Res Bull* 1981;7:519–579.
3. McKinnon GC. Ultrafast interleaved gradient-echo-planar imaging on a standard scanner. *Magn Reson Med* 1993;30:609–616.
4. Butts K, Riederer SJ, Ehman RL, Felmler JP, Grimm RC. Echo-planar imaging of the liver with a standard MR imaging system. *Radiology* 1993;189:259–264.
5. Butts K, Riederer SJ, Ehman RL, Thompson RM, Jack CR. Interleaved echo planar imaging on a standard MRI system. *Magn Reson Med* 1994;31:67–72.
6. Tan SG, Song AW, Wong EC, Hyde JS, Li SJ. High resolution fMRI with interleaved EPI. In: *Proceedings of the 3rd Annual Meeting of ISMRM, Nice, France, 1995*. p 796.
7. Menon RS, Ogawa S, Tank DW, Uğurbil K. 4 Tesla gradient recalled echo characteristics of photic stimulation-induced signal changes in the human primary visual cortex. *Magn Reson Med* 1993;30:380–386.
8. Farzaneh F, Riederer SJ, Pelc NJ. Analysis of T2 limitations and off-resonance effects on spatial resolution and artifacts in echo-planar imaging. *Magn Reson Med* 1990;14:123–139.
9. Haacke EM, Brown RW, Thompson MR, Venkatesan R. *Magnetic resonance imaging: physical principles and sequence design*. New York: John Wiley & Sons, Inc.; 1999.
10. Bandettini PA, Jesmanowicz A, Wong EC, Hyde JS. Processing strategies for time-course data sets in functional MRI of the human brain. *Magn Reson Med* 1993;30:161–173.
11. Edelstein WA, Bottomley PA, Pfeifer LM. A signal-to-noise calibration procedure for NMR imaging systems. *Med Phys* 1984;11:180–185.
12. Henkelman RM. Measurement of signal intensities in the presence of noise in MR images. *Med Phys* 1985;12:232–233.
13. Weisskoff RM, Baker J, Davis TL, Kwong KK, Cohen MS, Rosen BR. Power spectrum analysis of functionally weighted MR data: what's in the noise? In: *Proceedings of the 12th Annual Meeting of SMR, New York, 1993*. p 7.
14. Biswal B, Yetkin FZ, Haughton VM, Hyde JS. Functional connectivity in the motor cortex of resting human brain using echo-planar MRI. *Magn Reson Med* 1995;34:537–541.
15. Biswal B, Hudetz AG, Yetkin FZ, Haughton VM, Hyde JS. Hypercapnia reversibly suppresses low-frequency fluctuations in the human motor cortex during rest using echo-planar MRI. *J Cereb Blood Flow Metab* 1997;17:301–308.
16. Biswal B, Van Kylen JS, Hyde JS. Simultaneous assessment of flow and BOLD signals in resting-state functional connectivity maps. *NMR Biomed* 1997;10:165–170.
17. Hyde JS, Biswal BB. Functionally related correlations in the noise. In: Moonen C, Bandettini PA, editors. *Medical radiology: diagnostic imaging and radiation oncology*. Berlin, Heidelberg, New York: Springer-Verlag; 1999. p 263–275.
18. Hyde JS, Biswal BB, Jesmanowicz A. Echo-planar fMRI with 1-mm cubicle voxels. In: *Proceedings of the 7th Annual Meeting of ISMRM, Philadelphia, 1999*. p 1684.
19. Hyde JS, Biswal BB, Jesmanowicz A. Testing of a model for the fMRI contrast-to-noise ratio. In: *Proceedings of the 7th Annual Meeting of ISMRM, Philadelphia, 1999*. p 1729.
20. Biswal BB, Hyde JS. Pixel-wise correlation of fMRI signal with low-frequency physiological fluctuation intensity. In: *Proceedings of the 7th Annual Meeting of ISMRM, Philadelphia, 1999*. p 274.
21. Hyde JS, Biswal BB, Jesmanowicz A. Optimum voxel size in fMRI. In: *Proceedings of the 8th Annual Meeting of ISMRM, Denver, 2000*. p 200.
22. Prieto TE. Acoustic noise levels in head gradient coils during EPI as a function of frequency encoding direction. In: *Proceedings of the 7th Annual Meeting of ISMRM, Philadelphia, 1999*. p 105.
23. Cox RW. AFNI: software for analysis and visualization of functional magnetic resonance neuroimages. *Comput Biomed Res* 1996;29:162–173.
24. Cox RW, Hyde JS. Software tools for analysis and visualization of FMRI data. *NMR Biomed* 1997;10:171–178.
25. Cox RW. Medical College of Wisconsin, Milwaukee, WI. The MCW AFNI User Manual is available on www.biophysics.mcw.edu or from R.W. Cox.
26. Cox RW, Jesmanowicz A. Real-time 3D image registration for functional MRI. *Magn Reson Med* 1999;42:1014–1018.
27. Yablonsky D, Haacke EM. Theory of NMR signal behavior in magnetically inhomogeneous tissues: the static dephasing regime. *Magn Reson Med* 1994;32:749–763.
28. Narayanan A, Hartman JS, Bain AD. Characterizing nonexponential spin-lattice relaxation in solid-state NMR by fitting to the stretched exponential. *J Magn Reson* 1995;112A:58–65.
29. Pfenninger S, Antholine WE, Barr ME, Hyde JS, Kroneck PMH, Zumft WG. Electron spin-lattice relaxation of the [Cu(1.5)...Cu(1.5)] dinuclear copper center in nitrous oxide reductase. *Biophys J* 1995;69:2761–2769.
30. Cox RW, Jesmanowicz A, Hyde JS. Real-time functional magnetic resonance imaging. *Magn Reson Med* 1995;33:230–236.